Transient Suppression of Pulsed Ion Flux Induced by Dynamic Recycling in the Upgraded Linear Plasma Device TPD-II

Yuki HAYASHI[1)]*, Yukinori HAMAJI[2,3)], Noriyasu OHNO[4)], Naomichi EZUMI[5)], Shinichi NAMBA[6)], Shin KAJITA[1)], Akira TONEGAWA[7)], Makoto TAKAGI[4)], Goro NOMURA[2)], Sakuji KOBAYASHI[8)], Suguru MASUZAKI[2,3)]

[1)] *Graduate School of Frontier Sciences, The University of Tokyo, Kashiwa 277-8561, Japan*
[2)] *National Institute for Fusion Science, National Institutes of Natural Sciences, Toki 509-5292, Japan*
[3)] *The Graduate University for Advanced Studies, SOKENDAI, Toki 509-5292, Japan*
[4)] *Graduate School of Engineering, Nagoya University, Nagoya 464-8603, Japan*
[5)] *Plasma Research Center, University of Tsukuba, Tsukuba 305-8577, Japan*
[6)] *Graduate School of Advanced Science and Engineering, Hiroshima University, Hiroshima 739-8527, Japan*
[7)] *Global Research Institute of Nuclear Energy, Tokai University, Hiratsuka 259-1292, Japan*
[8)] *Kyoto Fusioneering Ltd., Tokyo 143-0006, Japan*

(Received 17 November 2025 / Accepted 29 January 2026)

The linear plasma device TPD-II was reactivated and upgraded to enable pulsed plasma and liquid-metal flow experiments. As an initial study, we performed pulsed plasma experiments using a capacitor bank system, focusing on the influence of transient recycling particles. Time-resolved measurements showed that the ion current at the target responded on a time scale longer than that of the pulse duration, attributed to slower transport of ions compared to that of electrons. In contrast, floating potentials responded on the same time scale as the pulse, reflecting the behavior of fast electrons. At higher pulse power, a transient drop in ion current and an increase in floating potential were observed after the input of pulse to the target, suggesting a rapid decrease in electron temperature and the onset of electron-ion recombination. Filtered high-speed imaging revealed enhanced He I emissions due to the recombination processes at the period. These results demonstrate the utility of the upgraded TPD-II in exploring transient plasma-neutral interactions relevant to divertor physics in future fusion reactors.

Keywords: linear plasma device, direct current arc discharge, pulse plasma, recycling particles

DOI: 10.1585/pfr.21.1402025

1. Introduction

In the development of a demonstration fusion reactor, the design of heat load handling scenarios for the divertor is of great importance. The divertor is exposed not only to steady-state heat loads but also to transient heat loads induced by plasma instability such as edge localized modes (ELMs) [1]. Under the ELMy H-mode conditions in ITER, pulsed heat loads reaching GW m^{-2} are expected [2]. For investigating the complex phenomena expected under the severe divertor heat load environment of a demonstration reactor, fundamental experiments using linear plasma devices provide an effective approach. Atomic and molecular processes during pulsed plasma superimposition as well as interactions with transient recycling particles have been studied in NAGDIS-II [3] and Magnum-PSI [4–6]. To further advance previous studies, it is necessary to investigate transient plasma–neutral interactions under conditions where the influence of recycling neutrals is more pronounced.

Although Magnum-PSI can generate high-power pulses similar to ELMs and has significantly contributed to the understanding of plasma-surface interactions under reactor-relevant conditions, further investigations are necessary under different boundary conditions to complement existing findings. In particular, in devices with large chamber volumes such as Magnum-PSI, scattered neutral particles tend to be lost before significantly affecting the plasma, which differs from the closed geometry of baffled divertors where neutrals can be more effectively confined. In addition, operating at as low a neutral pressure, P_n, as possible is favorable for enhancing recycling effects. In this study, we developed a linear plasma device capable of producing high-energy pulses that can be superimposed onto a steady-state plasma with an electron density, n_e, of $\sim 10^{19}$ m^{-3} under compact and low-P_n conditions, enabling clear observation of the effects of recycling neutrals on transient plasmas.

As an alternative to solid divertors, the use of liquid-metals at the plasma-material interface has been proposed [7].

*Corresponding author's e-mail: hayashi.yuki@k.u-tokyo.ac.jp

While liquid-metals offer high heat removal capability, several scientific challenges remain for their application in future fusion reactors. These include plasma-liquid interactions [8], the improvement of wettability [9], and the generation of impurities [10]. Such issues can be investigated using linear plasma devices. In particular, to study gas absorption, transport, and re-emission processes induced by interactions between flowing liquid-metals and plasmas, experimental setups capable of capturing dynamic plasma-liquid interactions are required.

In this study, the linear plasma device TPD-II was reactivated and upgraded to enable both pulsed plasma and liquid-metal flow experiments. As initial results, this paper reports the effects of pulsed plasma superimposed on a steady-state plasma using a capacitor bank system, with particular attention to transient recycling particles.

2. Experimental Setup

2.1 Linear plasma device TPD-II

The TPD-II device generates a steady-state plasma using TPD (Test Plasma by Direct-current discharge) type plasma source [11]. Around the year 2000, several divertor plasma studies were carried out in the device, mainly focusing on the double electron capture process, the closed divertor, and impurity transport [12–20]. After more than a decade of shutdown period, reactivation work was carried out. During this process, several upgrades and installations were implemented, including a newly designed plasma source, an upgraded pumping system, integration of the capacitor bank and a liquid-metal flow system, and the basic diagnostic system using Langmuir probes. A gas-driven liquid-metal flow system has been developed [9] and installed on the TPD-II device, and its details will be reported in another paper.

Figure 1 shows a picture and schematic view of the TPD-II device. TPD-II consists of a cylindrical glass chamber with an inner diameter of 143 mm and a total length of ~ 3 m, evacuated by three turbomolecular pumps (TMPs). The magnetic field strength can reach up to 0.6 T, while it was ~ 0.1 T in the present study. Helium (He) was used as the discharge gas. The plasma is terminated by a target plate located at z = 2.31 m, where z denotes the axial distance from the anode surface. The target plate is made of stainless steel for liquid-metal flow experiments, and a bias voltage of −100 V is applied to measure the total ion current into the target, I_{target}. A capacitance gauge installed at the same z position as the target plate is used to measure P_n. Throughout this study, P_n remained almost unchanged at ~ 0.3 Pa. Two Langmuir probes are located at z = 0.514 and 2.29 m. Both probes used cylindrical tungsten electrodes and were scanned as a function of radial position, r. The upstream probe located at z = 0.514 m was used to measure the $I - V$ characteristics and had an electrode with a diameter of 0.5 mm and a length of 1.0 mm. The downstream probe at z = 2.29 m was used to measure the ion saturation current into the probe, I_{probe}, at the plasma center by applying a bias of −100 V. The probe electrode had a diameter of 0.5 mm and a length of 0.5 mm. The dynamic behavior of the emission is observed using a high-speed camera (Phantom V7.0) installed at z = 1.484 m. The frame rate and exposure time were set to 10,000 fps and 97 μs, respectively. The frame size and pixel resolution were 64 × 256 and ~ 0.41 mm pixel^{-1}. Two optical filters were installed in front of the high-speed camera lens to observe line emission spectra. One was centered at the wavelength of 589 nm with a bandwidth of 10 nm to capture the He I emission due to the transition from the lower excited states with n = 3 (587.6 nm: $2^3P - 3^3D$), where n is the principal quantum number. The other was centered at 405 nm with a bandwidth of 10 nm to capture the He I emission due to the transition from the higher excited states with n = 5 (402.6 nm: $2^3P - 5^3D$).

2.2 Plasma source

Figure 2(a) shows a cross-section of the plasma source. The design is based on the plasma source used in the NAGDIS-II device [21]. An LaB_6 disk cathode with a diameter of 80 mm and thickness of 4 mm is heated by thermal radiation from a carbon (C) heater to emit thermionic electrons. The distance between the LaB_6 cathode and the C heater is 7 mm. The LaB_6 cathode is composed of four 90-degree fan-shaped segments to mitigate thermal stress caused by temperature gradients, which could otherwise lead to cracking due to the low thermal conductivity of LaB_6. A direct current (DC) arc discharge is generated by applying a discharge voltage, V_{src}, between the LaB_6 cathode and a copper (Cu) anode.

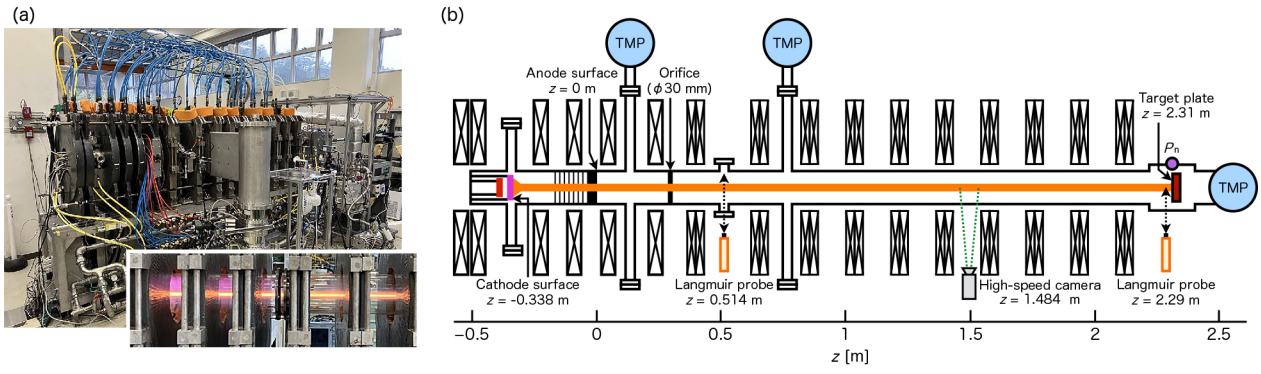

Fig. 1. (a) Picture and (b) schematic view of the linear plasma device TPD-II.

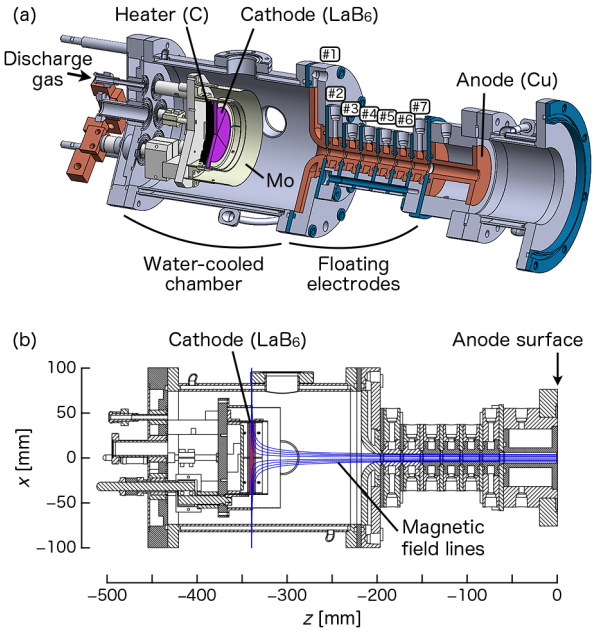

Fig. 2. (a) Cross-section of the DC arc plasma source and (b) magnetic field lines in the plasma source.

In this study, the discharge current, I_{src}, and V_{src} were 50 A and 138 V, respectively. The LaB_6 cathode is mounted using a cylindrical molybdenum (Mo) holder, which is connected to V_{src}. Outside of this holder, a Mo radiation shield is installed to reduce thermal radiation loss from the cathode. Since the shield is floating, it also suppresses undesired discharges between the cathode and the vacuum chamber wall. Pure He gas was supplied to the plasma source at a flow rate of 170 sccm. An additional 30 sccm of He was introduced from the position at z = 0.124 m, which is downstream of the anode, because gas injection from this location provided more stable discharge. Seven floating electrodes are placed between the cathode and the anode. These electrodes are mutually isolated and individually water-cooled. During the initiation of the discharge, all floating electrodes are grounded. Subsequently, they are floated sequentially from electrode #1 to #7, thereby forming a discharge path between the cathode and the anode. The inner diameter of the floating electrodes is 8 mm, while that of the anode is 12 mm. Figure 2(b) shows the magnetic field lines inside the plasma source. A cusp magnetic configuration is formed in front of the cathode, and the field converges toward the anode, contributing to the high density plasma generation.

The heating power, P_{heat}, required for the LaB_6 cathode to achieve sufficient thermionic electron emission depends on several geometrical factors, including the diameter and thickness of the LaB_6 disk, as well as its distance from the heater. Therefore, a heating test was conducted to investigate the relationship between P_{heat} and the surface temperature of LaB_6 in the present plasma source. Figure 3(a) shows the setup of the heating test. In a vacuum environment, P_{heat} up to 2.7 kW with the heating current, I_{heat}, up to 70 A was supplied to the C heater, and the surface temperature of the LaB_6

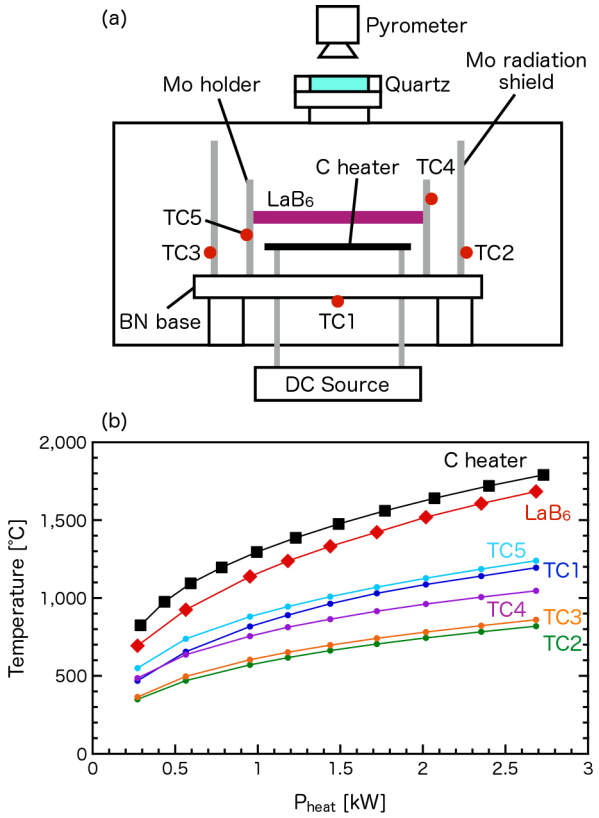

Fig. 3. (a) Schematic of the heating test setup and (b) P_{heat} dependence of the temperatures.

disk was measured using a two-color pyrometer through a quartz window. The vacuum chamber was water-cooled in the same manner as during actual plasma operation. The highest temperature was not observed at the geometric center of the cathode with r of 0 mm, rather near the center of one LaB_6 segment. Therefore, the pyrometer was aligned with the peak temperature location. The temperature difference between the peak region and the edge of the segment was ~ 60°C at P_{heat} = 2.7 kW. The temperature of the C heater was also measured by removing one LaB_6 segment. In addition, the temperatures of the surrounding components were measured with five K-type thermocouples (TCs). TC1 was mounted on the backside of the boron nitride (BN) base; TC2 and TC3 were placed symmetrically on the outer radial side of the Mo radiation shield; TC4 and TC5 were installed on the outer radial side of the Mo cathode holder, 6 mm downstream (anode side) and 10 mm upstream (opposite to the anode side) from the LaB_6 surface, respectively. Figure 3(b) shows the P_{heat} dependence of the temperatures. At P_{heat} = 2.7 kW, the surface temperature of the LaB_6 reached 1,680°C, while the C heater reached 1,790°C. Although the surrounding structures were also heated, the LaB_6 cathode was most efficiently heated. Since an LaB_6 surface temperature of 1,500°C was sufficient for initiating He plasma discharge, P_{heat} of 2.0 kW was adopted for the experiments in this study. After discharge initiation, the cathode was further heated by the plasma itself as I_{src} increased, which required P_{heat} to be reduced to below 1.0 kW in order to suppress LaB_6 erosion.

2.3 Pulsed plasma generation

Figure 4 shows the discharge circuit. In parallel with the DC power supply used for steady-state plasma generation, a capacitor bank (CB) system was installed to transiently enhance the discharge power, P_{src}. The CB system consisted of eight identical sections. Each section included a capacitor with an electrostatic capacitance of 480 μF, an inductor with an inductance of 20 μH, and an anti-reversal diode. Although not shown in the figure, the CB system was also equipped with a dedicated charging circuit for the capacitors. The stored energy in the capacitors was released through thyristor switching into the plasma through ohmic heating. The maximum capacitor voltage, V_{pulse}, was 1 kV; in this study, V_{pulse} was varied between 200 and 500 V. An analog-digital converter (Yokogawa 720254) was used to acquire V_{src}, reduced by a voltage divider, and I_{src}, measured by a shunt resistor, over the entire period covering before, during, and after the pulse. An 0.1 Ω shunt resistor also serves to stabilize the DC discharge.

3. Experimental Results

3.1 Steady-state plasma parameters

Figure 5 shows the radial profiles of n_e and electron temperature, T_e, measured by the Langmuir probe at z = 0.514 m, with I_{src} varied among 30, 40, and 50 A. The FWHM of the n_e profile was ~ 15 mm, which is wider than the diameter of the floating electrodes. This broadening is considered to be caused by diffusion. An increase in I_{src} led to a corresponding increase in both n_e and T_e. At I_{src} = 50 A, the peak values at the center reached ~ 2 × 10^{19} m^{-3} for n_e and 6 eV for T_e.

3.2 Discharge waveforms during pulse

Figure 6 shows the temporal evolutions of V_{src}, I_{src}, and P_{src} during pulse discharge. The trigger time of the pulse corresponds to t = 0 ms. Here, P_{src} is defined as the product of V_{src} and I_{src}. For V_{pulse} values of 300 and 500 V, transient increases in V_{src} and I_{src} resulted in enhancements in P_{src} of ~ 23 and 90 kW, respectively.

3.3 Temporal characteristics of ion current response to pulsed power input

Figure 7 shows the time evolutions of P_{src}, I_{probe} at z = 2.29 m, and I_{target} under various V_{pulse} conditions ranging from 200 to 500 V. Data acquisition during the pulse was performed 24 times under the same V_{pulse} conditions, and all waveforms were conditional-averaged to ensure high reliability. After the pulse was initiated, both I_{probe} and I_{target} increased compared to their steady-state values, indicating an enhancement of n_e during the pulse. The magnitude of these increases became larger with increasing V_{pulse}, reaching ~ 2–3 times the steady-state values at V_{pulse} = 500 V. Although the pulse width indicated by P_{src} was less than 1 ms, both I_{probe} and I_{target} exhibited longer responses of ~ 5–6 ms. In addition, a transient drop in I_{probe} and I_{target} was observed before

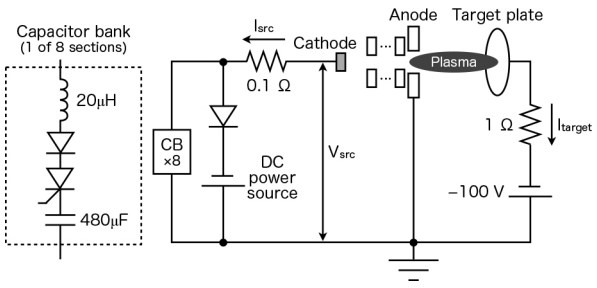

Fig. 4. Discharge circuit for compatible operation of steady-state DC discharge and transient pulse by a CB system.

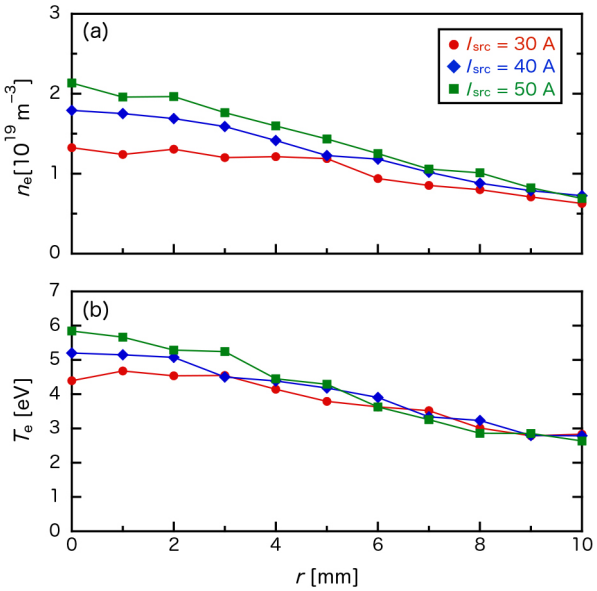

Fig. 5. Radial profiles of (a) n_e and (b) T_e measured by the Langmuir probe at z = 0.514 m with I_{src} of 30, 40, and 50 A.

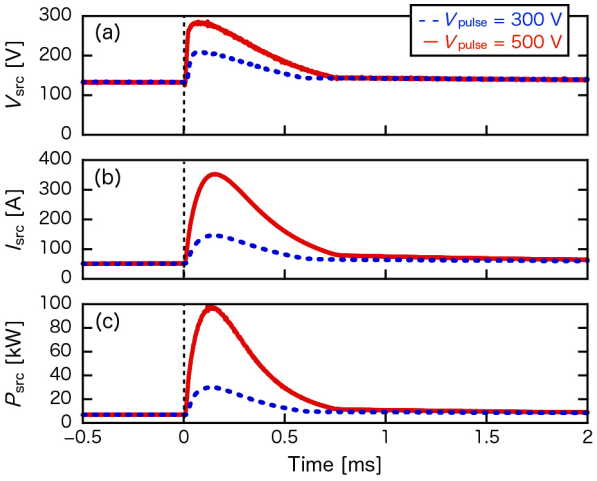

Fig. 6. Time traces of (a) V_{src}, (b) I_{src}, and (c) P_{src} during a pulse at V_{pulse} of 300 and 500 V. The trigger time of the pulse is defined as t = 0 ms.

their maximum values in cases where $V_{pulse} \geq 400$ V. This transient drop was not evident under lower V_{pulse} conditions. Since P_{src} exhibits a round-shape waveform, the pulsed plasma generated near the source region did not have such a transient

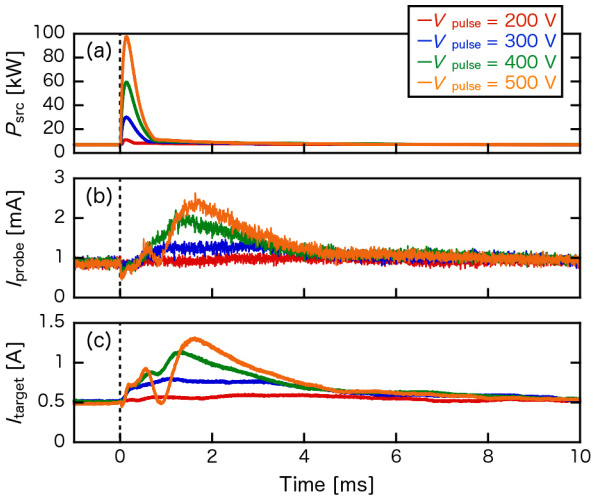

Fig. 7. Time evolutions of (a) P_{src}, (b) I_{probe} at z = 2.29 m, and (c) I_{target} during the pulse for various V_{pulse} values ranging from 200 to 500 V.

loss, and the observed attenuation was likely influenced during its propagation. The transient reduction of ion fluxes at $t \sim 1$ ms is discussed in detail in Sec. 4, with a focus on the influence of recycling neutrals on plasma parameters and atomic processes.

3.4 Transient response of floating potential to pulsed plasmas

Figures 8(a) and (c) show the floating potentials of the floating electrodes during the pulse. Under the steady-state plasma conditions, the floating potentials gradually become high from electrode #1 to #7, indicating a continuous potential gradient from the cathode to the anode. When the pulse is superimposed, the continuous potential distribution from the electrode #1 to #7 remains unchanged. However, the floating potentials of all electrodes deepen, suggesting an increase in T_e in the source region. The pulse duration shown by the floating potential response was less than 1 ms, and unlike I_{probe} and I_{target}, it did not exhibit a prolonged response at the floating electrodes.

Figures 8(b) and (d) show the floating potentials measured by the Langmuir probe at z = 2.29 m and r = 0 mm and the target plate. The decrease in floating potentials caused by the pulse input continued for less than 1 ms at the probe and the target, consistent with the behavior of the floating electrodes. Although the distance between the Langmuir probe and the target plate is only 20 mm, the floating potential at the probe was lower than that at the target. This is likely because the probe measures the plasma center, whereas the target integrates signals over a broader region.

The above results indicate that the floating potential responds on a time scale comparable to P_{src}. The difference in response time observed in the floating potential and ion flux might be attributed to the different behaviors of electrons and ions. This point will be discussed in Sec. 4. Figure 8(d) shows that, at V_{pulse} = 500 V, both the probe and the target plate exhibited a period in which the potential became higher than that in the steady-state phase after the negative peaks at $t \sim 1$ ms. This behavior implies a temporary decrease in T_e compared with the steady-state phase and will be discussed in Sec. 4 along with the transient suppression of I_{probe} and I_{target}.

3.5 Observation of atomic processes using a filtered high-speed camera

Figure 9 shows the time evolution of the emission intensity observed by the high-speed camera for V_{pulse} = 300 and 500 V, including total emission (w/o filter), low-n emission

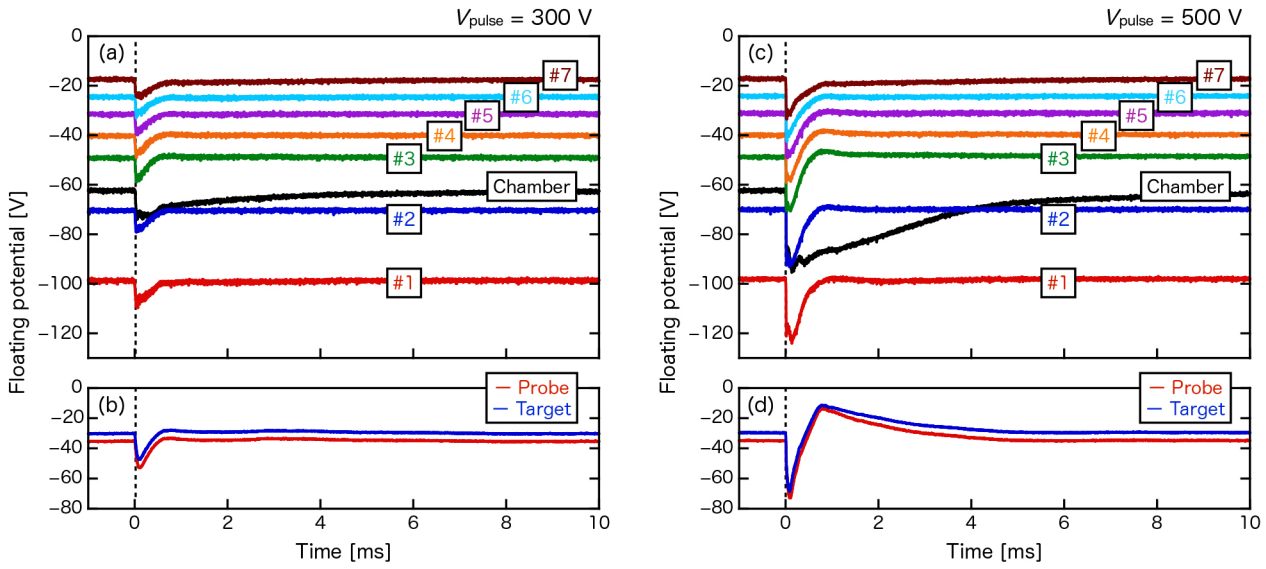

Fig. 8. Time evolutions of floating potentials of (a) and (c) the floating electrodes of the plasma source and (b) and (d) the Langmuir probe at z = 2.29 m and the target plate with V_{pulse} of 300 and 500 V, respectively. The label "Chamber" is the water-cooled chamber surrounding the cathode shown in Fig. 2(a).

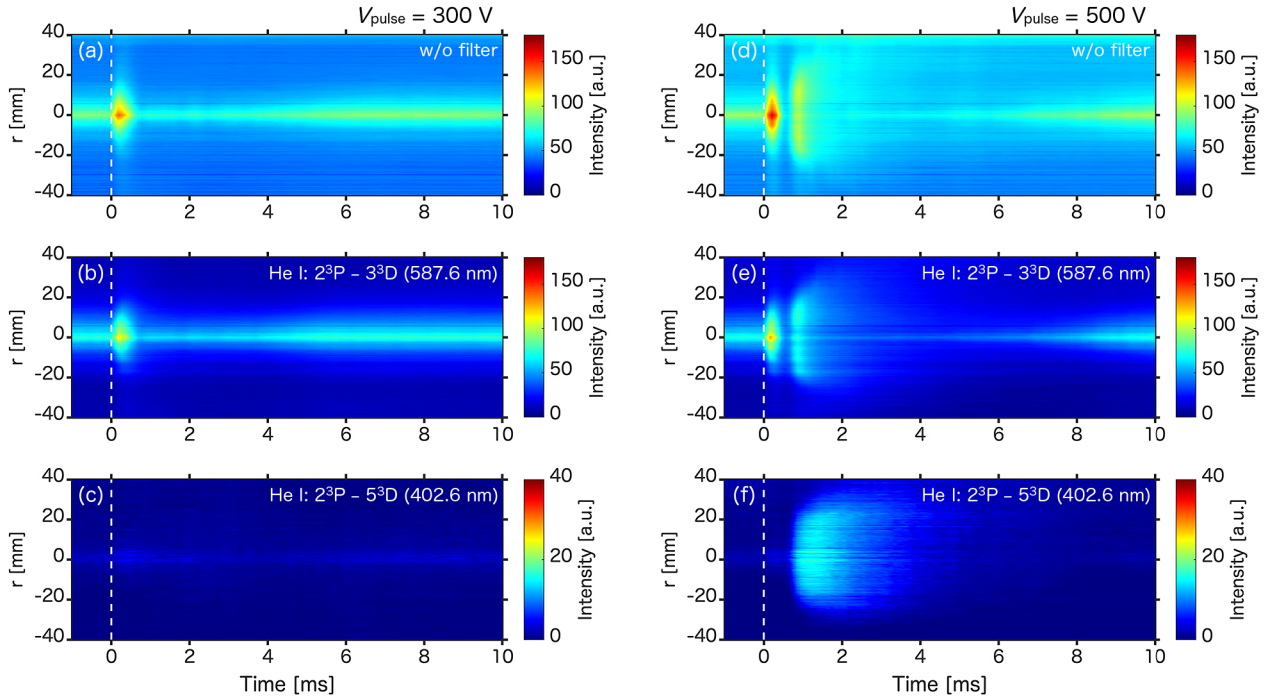

Fig. 9. Time evolutions of radial profiles of (a, d) total emission (w/o filter), (b, e) low-n emission (He I: 2^3P–3^3D), and (c, f) high-n emission (He I: 2^3P–5^3D) at V_{pulse} = (a-c) 300 and (d-f) 500 V, respectively.

(He I: 2^3P–3^3D), and high-n emission (He I: 2^3P–5^3D). The z-axis corresponds to the central pixel in the view, and the radial emission profiles at each time frame are extracted and arranged along the t axis. The data were averaged over eight pulses. For V_{pulse} = 500 V, the pulsed discharge was not stable. Therefore, the flow rate of discharge gas was increased from 170 to 200 sccm only for the high-speed camera measurements at 500 V. Since the discharge waveforms during the pulse remained the same, qualitative comparisons are considered valid.

Figure 9(a) shows that, for V_{pulse} = 300 V, a strong emission is observed by the pulsed plasma onset, followed by a narrowing of the plasma column. The low-n emission shown in Fig. 9(b) indicated similar trend, and the high-n emission in Fig. 9(c) was weak. This suggests that the response in the total emission to the pulse is mainly determined by the direct excitation processes to the lower-excited states. Figure 9(d) shows, for V_{pulse} = 500 V, the strong emission at pulse onset and subsequent plasma narrowing, similar to the 300 V case. However, two differences are identified in V_{pulse} = 500 V case: a second emission peak appears around t = 1 ms, and the duration of the plasma narrowing and attenuation is longer. The first emission peak shows a similar trend to the low-n emission in Fig. 9(e), suggesting that excitation to lower-excited states was dominant similar to the case at 300 V. In contrast, at the timing of the second emission peak, Fig. 9(f) shows that high-n emission is also observed, suggesting that a number of atoms in higher-excited states are generated at that moment.

4. Discussion

4.1 Increase in temporal width of ion current during pulses

The experimental results revealed that the response durations of I_{probe} and I_{target} were longer than the pulse width indicated by P_{src}, as shown in Fig. 7. In contrast, the floating potential measurements obtained from the floating electrodes, probe, and target plate showed that the floating potentials at all positions responded on the same time scale as P_{src}, as shown in Fig. 8. This indicates that only the ion fluxes, as represented by I_{probe} and I_{target}, responded more slowly.

When pulsed V_{src} is applied, high-energy electrons are generated from the plasma source, and some electrons can reach the target plate, contributing to the observed reduction in the floating potential. Such energetic electrons have also been observed at the beginning of ELMs and have been discussed in JET [22]. Because these energetic electrons are transported rapidly, the pulse widths indicated by P_{src} and the floating potential at the target are identical. However, some of these high-energy electrons can ionize background He atoms. Under high P_n conditions, their influence is known not to appear as enhanced ionization but rather as a suppression of recombination processes [3, 23]. In this study, since P_n was low ($\sim$ 0.3 Pa) and the plasma was not in a recombining state under steady-state conditions, it is expected that n_e increases along the entire path from the anode to the target due to ionization by high-energy electrons. The ions produced by ionization are transported toward the target at a velocity significantly lower than that of electrons, typically on the order of 10–20% of the ion sound speed, C_s [24–27]. Assuming a

bulk $T_e \sim 6$ eV, C_s is estimated to be ~ 9,400 m/s. Given the 2.31 m distance between the anode and the target, ions traveling at 10–20% of C_s would require roughly 1–2 ms to reach the target. The observed response time of I_{target} was ~ 6 ms, slightly longer. However, this can be reasonably explained by the presence of low-T_e plasma components in the periphery, which would reduce C_s. Therefore, the difference in response duration of I_{probe} and I_{target} from P_{src} is attributed to the difference in transport time between electrons and ions.

4.2 Transient attenuation of ion flux under high pulsed power conditions

From the experiments, both I_{probe} and I_{target} increased at the pulse onset but showed a transient suppression before reaching their peak values, as shown in Figs. 7(b) and (c). This behavior appeared only under high V_{pulse} conditions. The suppression of ion flux occurred at $t \sim 1$ ms, at which the floating potential at the unbiased target became higher than that under steady-state conditions, as shown in Fig. 8(d). This increase in the floating potential suggests a reduction in T_e after the pulse arrival. In He plasmas, T_e below 1 eV enhances electron-ion recombination (EIR) [28–30], which neutralizes ions, resulting in the I_{target} decrease. In recombining plasma, the population of high-n states is likely to be determined by the EIR processes. Therefore, high-n emissions are indicators of EIR processes [31]. Filtered high-speed camera measurements revealed the presence of highly excited atoms during the second emission peak at $t \sim 1$ ms only when $V_{pulse} = 500$ V, implying that T_e may have been sufficiently decreased to trigger the EIR processes. To reduce T_e, enhancement of plasma-neutral interactions is necessary, but the current background $P_n \sim 0.3$ Pa is insufficient. A plausible explanation is that the pulsed plasma input in the target generated a substantial number of recycling particles, causing the target to act as a transient neutral gas source. This could locally increase P_n near the target immediately after the onset of the pulse. Moreover, the amount of recycling is likely to be greater at higher V_{pulse}, resulting in a significant contribution. The stronger and longer suppression of the emission after the pulse input at $V_{pulse} = 500$ V is likely due to the generation of more recycling neutrals, which have a greater impact on plasma. Even at $V_{pulse} = 300$ V, although EIR processes are not triggered, the emission intensity decreases and the emission region narrows due to plasma cooling caused by recycling neutrals. The duration of the suppression is considered to be determined by the residence time of these neutrals before being evacuated.

Similar effects have been observed in Magnum-PSI experiments, where recycling particles produced by a pulsed plasma influenced subsequent pulses and truncated I_{target} [5]. These effects were observed only under low P_n conditions, indicating that momentum transfer from recycling particles directly to ions in the pulsed plasma plays a significant role when background neutrals are not sufficient to cause scattering. In Magnum-PSI, I_{target} increased by a factor of 10 during the pulse compared to the steady-state phase, suggesting substantial recycling during the pulse. In contrast, the increase in I_{target} by pulse in TPD-II was only a factor of 2 to 3, indicating a lower enhancement of recycling. Nevertheless, similar plasma behavior, i.e. the transient attenuation in the ion flux, was observed. This similarity, despite the difference in recycling magnitude, validates the design concept introduced in the present study. As intended, the compact chamber geometry (143 mm diameter) of TPD-II enabled the confinement of scattered recycling neutrals, which likely re-entered the plasma region and locally enhanced P_n. The low-P_n condition also highlighted the influence of recycling particles on transient plasma behavior. This setup successfully reproduced effects previously observed in Magnum-PSI, which has a much larger chamber (500 mm diameter [32]) and where scattered neutrals are more easily lost. Figure 10 shows a schematic illustration of temporary and localized enhancement of P_n immediately after the inflow of the pulsed plasma into the target. The observed behavior in TPD-II confirms that chamber geometry and neutral confinement strongly influence transient plasma-neutral interactions. The mechanism is comparable to that of closed divertor configurations, where baffle structures enhance local neutral density to promote plasma-neutral interactions [33]. Furthermore, in Magnum-PSI, the reduction in ion flux was observed only in a localized region near the target and not at the probe located 200 mm upstream. In contrast, the TPD-II experiment showed reductions in both I_{probe} and I_{target}, with the impact extending as far upstream as the high-speed camera position, suggesting a broader spatial impact. By considering the mean free paths, recycling neutrals emitted from the target are unlikely to be ionized before

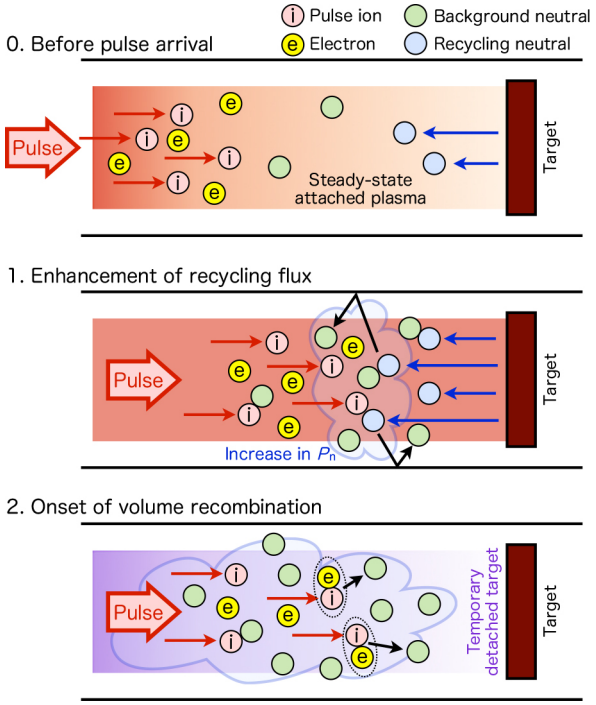

Fig. 10. Schematic illustration of the impacts of recycling neutral particles on the temporary increase in P_n, resulting in the suppresparsion of pulsed plasma by the EIR processes.

reaching the camera observation position but are likely to be scattered by collisions with pulsed ions. However, due to the effective confinement of neutral particles, it is considered plausible that the resulting increase in P_n can propagate upstream and influence the plasma behavior at the high-speed camera position. Because EIR processes play a significant role in mitigating heat fluxes [34–36], the phenomena revealed in this study may provide new insights into the issue of excessive heat loads on divertor targets. To further investigate the extent of the influence of recycling particles, future studies should include time-resolved measurements of P_n and high-speed camera diagnostics along the z direction to determine how far upstream these effects propagate.

5. Conclusions

The linear plasma device TPD-II was reactivated and upgraded to enable both pulsed plasma and liquid-metal flow experiments. As an initial investigation, experiments were conducted to examine the effects of pulsed plasma superimposed on steady-state plasma using a capacitor bank system. Langmuir probe and target plate measurements revealed that the temporal responses of the ion currents were longer than the pulse duration indicated by P_{src}, which can be attributed to the slower transport of ions compared to high-energy precursor electrons. At higher V_{pulse}, both I_{probe} and I_{target} exhibited transient attenuation before reaching their peak values, accompanied by a temporary increase in floating potential, suggesting a reduction in T_e and the onset of EIR processes. Filtered high-speed camera observations supported this interpretation through the detection of high-n He I emissions during the period. These results imply that a number of recycling particles generated at the target locally increased P_n immediately after the input of the pulsed plasma to the target, promoting plasma-neutral interactions and transient cooling.

The upgraded TPD-II device provides a new experimental platform for investigating transient plasma-neutral and plasma-material interactions under pulsed heat loads. These findings contribute to the fundamental understanding required for designing heat load control and mitigation schemes in future fusion reactors.

Acknowledgments

This work was supported by JSPS KAKENHI Grant Numbers JP22K14024 and JP23K13088. This work was performed with the support and under the auspices of the NIFS Collaboration Research Program (NIFS17KOAF005, NIFS25KIPT020, and NIFS25KIIT017). This work was (partly) supported by Foundation of Public Interest of Tatematsu.

[1] R. Pitts *et al.*, Nucl. Fusion **47**, 1437 (2007).
[2] A. Loarte *et al.*, Nucl. Fusion **54**, 033007 (2014).
[3] N. Ohno *et al.*, Phys. Plasmas **6**, 2486 (1999).
[4] Y. Li *et al.*, Plasma Phys. Control. Fusion **63**, 085016 (2021).
[5] Y. Hayashi *et al.*, Plasma Phys. Control. Fusion **64**, 105013 (2022).
[6] Y. Hayashi *et al.*, Nucl. Fusion **65**, 086013 (2025).
[7] M. Abdou *et al.*, Fusion Eng. Des. **54**, 181 (2001).
[8] K. Sasaki and H. Koyama, Appl. Phys. Express **11**, 036201 (2018).
[9] Y. Hamaji *et al.*, Fusion Eng. Des. **210**, 114727 (2025).
[10] G.G. Van Eden *et al.*, Phys. Rev. Lett. **116**, 135002 (2016).
[11] M. Otsuka *et al.*, J. Quant. Spectrosc. Radiat. Transfer **15**, 995 (1975).
[12] T. Oda *et al.*, J. Nucl. Mater. **241–243**, 1238 (1997).
[13] S. Namba *et al.*, Fusion Eng. Des. **34–35**, 777 (1997).
[14] S. Namba *et al.*, J. Nucl. Mater. **266–269**, 1157 (1999).
[15] S. Namba *et al.*, J. Appl. Phys. **88**, 3182 (2000).
[16] A. Matsubara *et al.*, J. Plasma Fusion Res. **78**, 196 (2002).
[17] A. Matsubara *et al.*, J. Nucl. Mater. **313–316**, 720 (2003).
[18] A. Matsubara *et al.*, Plasma Fusion Res. SERIES **6**, 433 (2004).
[19] T. Sugimoto *et al.*, Plasma Fusion Res. SERIES **6**, 723 (2004).
[20] A. Matsubara *et al.*, J. Nucl. Mater. **337–339**, 181 (2005).
[21] N. Ohno *et al.*, Nucl. Fusion **41**, 1055 (2001).
[22] C. Guillemaut *et al.*, Nucl. Fusion **58**, 066006 (2018).
[23] H. Tanaka *et al.*, Phys. Plasmas **32**, 022504 (2025).
[24] S. Kado *et al.*, Contrib. Plasma Phys. **44**, 656 (2004).
[25] E.-K. Park *et al.*, Curr. Appl. Phys. **12**, 1497 (2012).
[26] Y. Hayashi *et al.*, Phys. Plasmas **23**, 012511 (2016).
[27] Y. Hayashi *et al.*, Phys. Plasmas **24**, 062509 (2017).
[28] N. Ohno *et al.*, Czech. J. Phys. **48**, 127 (1998).
[29] D. Nishijima *et al.*, J. Nucl. Mater. **290–293**, 688 (2001).
[30] H. Tanaka *et al.*, Phys. Plasmas **27**, 102505 (2020).
[31] D. Nishijima *et al.*, Plasma Phys. Control. Fusion **44**, 597 (2002).
[32] H.J. Van Der Meiden *et al.*, Rev. Sci. Instrum. **83**, 123505 (2012).
[33] L. Casali *et al.*, Nucl. Fusion **60**, 076011 (2020).
[34] A.W. Leonard *et al.*, Phys. Rev. Lett. **78**, 4769 (1997).
[35] Y. Hayashi *et al.*, Nucl. Fusion **56**, 126006 (2016).
[36] N. Ohno, Plasma Phys. Control. Fusion **59**, 034007 (2017).